The Journal of Chemical Physics

Assessment of mean-field microkinetic models for CO methanation on stepped metal surfaces using accelerated kinetic Monte Carlo

Cite as: J. Chem. Phys. **147**, 152705 (2017); https://doi.org/10.1063/1.4989511
Submitted: 20 April 2017 • Accepted: 08 June 2017 • Published Online: 28 June 2017

Mie Andersen, Craig P. Plaisance and Karsten Reuter

Assessment of mean-field microkinetic models for CO methanation on stepped metal surfaces using accelerated kinetic Monte Carlo

Mie Andersen,[a] Craig P. Plaisance, and Karsten Reuter
Chair for Theoretical Chemistry and Catalysis Research Center, Technische Universität München, Lichtenbergstr. 4, D-85747 Garching, Germany

(Received 20 April 2017; accepted 8 June 2017; published online 28 June 2017)

First-principles screening studies aimed at predicting the catalytic activity of transition metal (TM) catalysts have traditionally been based on mean-field (MF) microkinetic models, which neglect the effect of spatial correlations in the adsorbate layer. Here we critically assess the accuracy of such models for the specific case of CO methanation over stepped metals by comparing to spatially resolved kinetic Monte Carlo (kMC) simulations. We find that the typical low diffusion barriers offered by metal surfaces can be significantly increased at step sites, which results in persisting correlations in the adsorbate layer. As a consequence, MF models may overestimate the catalytic activity of TM catalysts by several orders of magnitude. The potential higher accuracy of kMC models comes at a higher computational cost, which can be especially challenging for surface reactions on metals due to a large disparity in the time scales of different processes. In order to overcome this issue, we implement and test a recently developed algorithm for achieving temporal acceleration of kMC simulations. While the algorithm overall performs quite well, we identify some challenging cases which may lead to a breakdown of acceleration algorithms and discuss possible directions for future algorithm development. *Published by AIP Publishing.* [http://dx.doi.org/10.1063/1.4989511]

I. INTRODUCTION

The computational screening of potential catalyst materials has been greatly facilitated by the development of scaling relations.[1–5] These relations allow for the prediction of important catalytic parameters such as adsorption energies and activation energies over the whole series of transition metals (TMs) based on a limited number of actual first-principles calculations. Traditionally, such screening studies have relied on microkinetic models based on the mean-field approximation (MFA), in which spatial correlations in the distribution of the reaction intermediates on the catalyst surface are neglected. While early MFA models used an assumed rate-determining step to derive an analytical expression for the reaction rate,[6] more recent models treat all reaction steps as potentially rate-determining and solve a set of coupled differential equations numerically for the surface coverages and rates.[7–9] It is commonly believed, though rarely actually tested, that MFA models are accurate representations of the system kinetics, when these kinetics are characterized by low barriers for diffusion and insignificant lateral interactions between the adsorbates. Since diffusion barriers of common adsorbates are typically low on metal catalysts (around 0.5 eV),[10] MF models disregarding lateral interactions have been extensively applied to study surface reactions on metals.[6,9,11] Recently, MFA models that account for finite lateral interactions through coverage-dependent adsorption energetics have also been developed.[7,12,13] The accuracy of such models remains, however, to be thoroughly benchmarked against more general methods that explicitly treat lateral interactions, for instance, through cluster expansion models.[14,15]

An alternative branch of microkinetic models avoids the MFA by making use of spatially resolved (lattice) kinetic Monte Carlo (kMC) simulations.[16–19] kMC simulations allow for the inclusion of detailed site-resolved lateral interactions between the adsorbates, using either site-blocking rules[20,21] or cluster expansion models.[22,23] However, even in the absence of lateral interactions, previous studies, for example, of CO oxidation on $RuO_2(110)$ have shown that kMC models may give a more accurate description of the system kinetics than a corresponding MFA model since the latter still neglects correlations in the spatial configuration of the adsorbates.[24,25] Such correlations were shown to be particularly important in the regime characterized by a high surface coverage of O species and could be traced to a relatively high barrier of 1.6 eV for O diffusion. Still, considering the typically lower diffusion barriers on metals, such findings have been considered to be uniquely associated with oxides or other compound materials.

In the present work, we challenge the assumption that MFA models disregarding lateral interactions generally provide an accurate description of surface catalytic reactions on metals. For this, we explicitly compare MFA and kMC simulations based on exactly the same adsorption energetics and reaction network. As a test case for this comparison, we choose CO methanation on stepped metal surfaces, which is a prototypical reaction model including various classes of surface reactions (dissociation/recombination and hydrogenation/dehydrogenation reactions) as well as different types of adsorption sites (step and terrace). A corollary of our endeavor is to demonstrate the applicability of kMC models to

[a]Electronic mail: mie.andersen@ch.tum.de

computational screening studies based on scaling relations. Such studies have typically been based on simpler MFA models since the focus lay more on screening a large space of potential catalyst materials for trends in the catalytic activity rather than giving as quantitative as possible an account of the activity of a given material. In contrast, previous kMC models have typically had the opposite focus. However, nothing prevents the use of energetic databases constructed from the more approximate scaling relations in kMC models as well. Our reaction model for CO methanation is therefore particularly inspired by the recent scaling-relation-based MFA study of Lausche *et al.*[7]

kMC models have the great advantage of allowing for a detailed spatial resolution of the system, both in the presence and absence of lateral interactions. Their main disadvantage is that the computational cost is significantly higher than for corresponding MFA models. This becomes especially problematic for surface reactions on metals due to the large disparity in the time scales of the processes considered. As already emphasized, these often range from very fast surface diffusion processes to very slow surface reactions. This causes kMC algorithms to spend all of the computational effort simulating the fast processes, while never reaching the time scales relevant for the slow processes. A typical work-around employed in previous kMC studies on metals is to artificially raise the barriers for diffusion to a computationally tractable level.[20–22] The validity of this approach, i.e., that it does not affect the outcome of the simulations, is straightforward as long as the study focuses on a single material and rather simple reactions such as CO oxidation, which contain at most a handful of different diffusion barriers. However, when we consider significantly more complicated reaction models such as CO methanation and employ scaling-relation-based models to consider not only one catalyst material but the whole series of TMs, such manual adjustment and verification of the used diffusion barriers quickly become intractable.

In the present work, we therefore aim for an alternative, automated treatment of the time scale disparity problem in kMC. Several methods proposed in the literature rely on a user-specified division of the processes into "fast" and "slow" reactions, where only the slow reactions are treated stochastically, while the fast reactions are treated deterministically or using a Langevin equation.[26,27] While we do rely on such an approach to describe H in our reaction model (*vide infra*), these methods are in general difficult to use for complex reaction models since we do not *a priori* know which processes can be reliably approximated as fast processes under steady state conditions. Chatterjee and Voter developed a temporal acceleration scheme that functions by modifying the rate constants of fast processes without the need for the user to specify these processes in advance.[28] While it seemed to perform well for simple toy models, the fact that it identifies processes based on the configuration of the entire system likely makes it too inefficient for complex reaction models, where the number of possible configurations is typically so large that many configurations may only be visited very rarely during the entire simulation. This problem was addressed in the recently developed alternative acceleration scheme by Dybeck, Plaisance, and Neurock,[29] where processes are instead grouped into reaction channels based on certain, flexible criteria. We therefore choose this method as the basis for accelerating our kMC model, but also discuss possible extensions towards the algorithm of Chatterjee and Voter.

Compared to the rather simple reaction model used to test the acceleration algorithm in Ref. 29, which could have equivalently been described in the MFA, our more complex scaling-relation-based reaction model provides for a much more thorough testing of the algorithm. Indeed, as we will show, such a complex reaction scheme does pose some unforeseen challenges for the algorithm. Additionally, we test the algorithm for a surface catalytic system involving diffusion, which was not included in the reaction model used in Ref. 29. We implemented the algorithm in our in-house kMC code kmos.[30] Owing to the high numerical efficiency of kmos, we are able to directly test the algorithm against non-accelerated kMC simulations for selected cases where the time scale disparity problem is less severe. It was speculated in Ref. 29 that the algorithm may not be applicable in systems where diffusion is slow and rate-limiting. By direct comparison to non-accelerated kMC, we show that it does give accurate results if diffusion is rate-limiting and slow enough that it is not significantly accelerated by the algorithm. However, we find the algorithm to underestimate the number of executions of fast diffusion processes necessary to correctly capture the system kinetics if diffusion is both fast and still rate-limiting.

II. MODELS AND METHODS

A. Reaction model and rate constants

To allow for a clean comparison of MFA and kMC, we base both models on exactly the same reaction model and the exact same underlying (scaling-relation-based) rate constants. The reaction model employed for CO methanation is similar to the model from Ref. 7. The only difference is that, whereas the previous study considered only the most stable adsorption site of each adsorbate, we consider here all stable adsorption sites of each adsorbate. Thus, our extended reaction model considers multiple reaction pathways with far fewer pre-existing assumptions about the preferred pathway. As in Ref. 7, we consider various TMs (Cu, Pd, Pt, Re, Rh, Ru) and three generic site types on the stepped (211) TM surface (cf. Fig. 1): the "step" site (*s*) is located on the upper part of the step, the "fourfold" site (*f*) is located at the lower part of the step, and the "terrace" site (*t*) is located in between the two step sites. From our density functional theory (DFT) calculations (cf. Sec. II C), we find that the fourfold coordinated *f* site is a stable adsorption site for C and CH species, while all adsorbates are stable on the *s* and *t* sites. In addition, hydrogen is adsorbed on a special "hydrogen reservoir" site (*h*), which has the same energetics as a *t* site, similar to the approach taken in Ref. 7 (cf. Sec. S4 in the supplementary material for more details).

In short and without yet specifying reaction sites, our reaction model includes CO and (dissociative) H_2 adsorption, H-assisted CO dissociation, C and CH_x hydrogenation

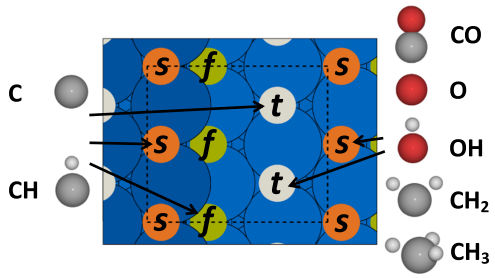

FIG. 1. Schematic of the upper step (s), lower fourfold (f), and terrace (t) sites offered by the stepped (211) surface as well as the supercell used for the DFT calculations (dashed black line). As indicated by the arrows, C and CH adsorb on all three sites, while CO, O, OH, CH_2, and CH_3 are only stable on the s and t sites. Note that the exact location of a site is only schematic. In reality, the locations of the s and t sites are either ontop, bridge, or hollow depending on the most stable adsorption site exhibited by the studied adsorbate on each metal.

steps up to CH_4 (followed by immediate desorption), hydroxyl disproportionation, and O and OH hydrogenation. Considering all site combinations, this leads to 24 different (non-diffusive) reaction steps. These steps are explicitly listed in Sec. S1.1 of the supplementary material. For every adsorbate, we also consider all possible diffusion processes between the stable adsorption sites. This leads to a total of 27 different diffusion steps, which are listed in Sec. S1.2 of the supplementary material. Note that diffusion between two sites of the same type is only considered explicitly in the kMC model, whereas the MFA model implicitly considers this type of diffusion to be so fast as to yield the perfect mixing in the adsorbate layer assumed in the MFA.

To determine the rate constants, different approximations are used depending on whether the reaction step is activated or not. CO adsorption is non-activated on all metals. Furthermore, H_2 adsorption is a very fast process compared to the typical rate-limiting step for CO methanation (CO dissociation). This allows us to also model this step as non-activated without loss of accuracy. The rate constant $k^{\mathrm{ad}}_{st,i}$ for non-activated adsorption onto the site st is the product of the local sticking coefficient $\tilde{S}_{st,i}$ and the rate of impingement of the gas-phase species i onto the site st of area A_{st},[31]

$$k^{\mathrm{ad}}_{st,i}(T,p_i) = \tilde{S}_{st,i}(T)\frac{p_i A_{st}}{\sqrt{2\pi m_i k_{\mathrm{B}} T}}. \tag{1}$$

Here T is the temperature, p_i and m_i are the pressure and mass of species i, respectively, and k_{B} is the Boltzmann constant. Lacking further detailed knowledge, $\tilde{S}_{st,i}$ is set to unity. In the case of activated adsorption (for H_2O and CH_4), the rate constants can be derived using transition state theory (TST),

$$k^{\mathrm{ad,TST}}_{st,i}(T,p_i) = \frac{A_{st}}{A_{uc}}\frac{k_{\mathrm{B}}T}{h}\exp\left(\frac{-\Delta G^{\mathrm{ad}}_{st,i}}{k_{\mathrm{B}}T}\right), \tag{2}$$

where $\Delta G^{\mathrm{ad}}_{st,i}$ is the free energy barrier for adsorption. When there are several adsorption sites within the unit cell area A_{uc}, the ratio of areas is a normalization factor reflecting the relative adsorption weight onto the site st. Here we simply assume that the active area for adsorption A_{st} is equal to half of the unit cell area for both the s and t adsorption sites. The desorption rate constants $k^{\mathrm{des}}_{st,i}$ follow from detailed balance, i.e.,

$$\frac{k^{\mathrm{ad}}_{st,i}(T,p_i)}{k^{\mathrm{des}}_{st,i}(T)} = \exp\left(\frac{\Delta G_{st,i}(T,p_i)}{k_{\mathrm{B}}T}\right), \tag{3}$$

where $\Delta G_{st,i}$ is the difference in free energy between the species i adsorbed on site st and the species i in the gas phase.

The rate constants for surface-bound processes such as surface reaction and diffusion, $k^{\mathrm{bound}}_{IS\to FS}$, are given by the TST expression

$$k^{\mathrm{bound,TST}}_{\mathrm{IS}\to\mathrm{FS}}(T) = \frac{k_{\mathrm{B}}T}{h}\exp\left(\frac{-\Delta G^{\mathrm{bound}}_{\mathrm{IS}\to\mathrm{FS}}}{k_{\mathrm{B}}T}\right), \tag{4}$$

where IS and FS are the initial and final states of the process, and $\Delta G^{\mathrm{bound}}_{\mathrm{IS}\to\mathrm{FS}}$ is the free energy barrier for the process. The latter consists of the energetic (DFT-calculated) part of the barrier $\Delta E^{\mathrm{bound}}_{\mathrm{IS}\to\mathrm{FS}}$ as well as the enthalpy/entropy corrections calculated from the vibrational frequencies of the initial state and the TS. Further details regarding the derivation of the rate constants can be found in Ref. 31.

Assuming diffusion to be fast, MFA models often neglect kinetic barriers for diffusion between different site types.[7] In this work, we aim to compare MF and kMC models, which makes an explicit description of diffusion barriers necessary. On Re(0001), diffusion barriers for the species involved in CO methanation have been calculated using DFT and were found to lie in the range 0.1–0.8 eV.[10] Since our reaction model contains more than 25 unique diffusion processes (cf. Sec. S1.2 in the supplementary material), the calculation of accurate barriers for all six TM surfaces for each diffusion process is computationally very demanding. As a first approximation, we therefore use the barriers calculated on Re(0001) in Ref. 10 for all TMs and neglect the enthalpy/entropy corrections to the TS energy. In order to ensure that the rate constants resulting from the diffusion barriers fulfill detailed balance, we model the barriers with a Brønsted-Evans-Polanyi (BEP) relationship

$$\Delta E^{\mathrm{diff}}_{st\to st',i} = \alpha * \Delta E_{st\to st',i} + \beta, \tag{5}$$

where $\Delta E^{\mathrm{diff}}_{st\to st',i}$ is the diffusion barrier for the species i to diffuse from any site st to any other site st', and $\Delta E_{st\to st',i}$ is the difference in the adsorption energy of species i between the two sites st and st'. The parameter α was fixed to 0.5 for all diffusion reactions, while the β value was fixed to the value of the barrier calculated for Re(0001).[10] For diffusion between two sites of the same type, $\Delta E_{st\to st',i}$ will be zero, i.e., in this case the diffusion barrier used corresponds to the value estimated for Re(0001). As discussed in Sec. III B in detail, as soon as diffusion barriers turned out to be critical for a correct estimation of the catalytic activity, we replace them by more accurate barriers calculated explicitly on all six TMs and using the correct stepped (211) geometry.

B. Scaling relations

It is well known that linear scaling relations exist between certain quantities such as the adsorption energies of CH_x species and C, OH_x species and O, or between TS energies

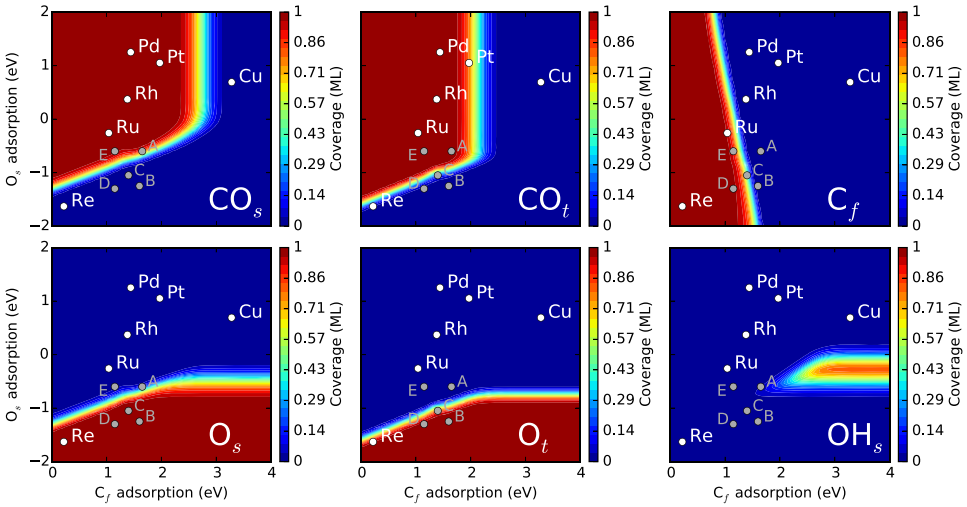

FIG. 2. MFA steady-state coverages of CO_s, CO_t, C_f, O_s, O_t, and OH_s as a function of the C_f and O_s adsorption energies. The C_f and O_s adsorption energies for the considered stepped metal (211) surfaces are indicated in white, while the descriptor points considered as test cases for the kMC simulations (*A*, *B*, *C*, *D*, and *E*) are indicated in grey. The reaction conditions are T = 523 K and p = 1 bar with a gas composition of 1% CO, 97% H_2, 1% CH_4, and 1% H_2O as in Ref. 7.

and the adsorption energies of the dissociated products on TM surfaces.[3,4] Such scaling relations also exist between the adsorption energy of a species on one site type (e.g., CO on the *s* site) and the adsorption energy of another species on a different site type (e.g., C on the *f* site).[7] By constructing scaling relations, we can effectively express the energetic data required for all the rate constants in the reaction model on a given TM in terms of only two so-called descriptors: the adsorption energy of C on the *f* site and the adsorption energy of O on the *s* site. This allows for the visualization of trends over the TM series in terms of only these two parameters (cf. Figs. 2–4) and can be used for the rapid screening of potential catalyst materials by calculating only the descriptors and not the full DFT dataset. The scaling plots and fitted scaling parameters from our own DFT calculations can be found in Sec. S2 of the supplementary material.

We also make use of scaling relations to reduce the overall number of TS energies that must be calculated in a multi-site kinetic model. The reaction model discussed in Sec. II A contains a total of 17 adsorption energies and 21 TS energies that must be determined on each of the six TM surfaces by DFT calculations. With the exception of CO dissociation, which is known to be feasible only at step sites,[32] most of the reaction steps are considered at several different sites. For these reaction steps, we found that the same TS scaling relation holds regardless of the site type on which the reaction occurs. This is exploited to estimate some TS energies directly from the scaling relations (cf. Sec. S2.3 of the supplementary material). This reduces the number of TS energies to be calculated on each metal from 21 to 14.

C. Density functional theory

The density functional theory calculations are performed with the plane-wave code Quantum ESPRESSO[33] (PWSCF v.5.0.2, svn rev. 10452) using ultrasoft pseudopotentials.[34] Electronic exchange and correlation effects are described using the BEEF-vdW functional,[35] which includes a correction to account for van der Waals interactions. The stepped (211) surfaces of Cu, Pd, Pt, Re, Rh, and Ru are modeled by nine-layer slabs, which corresponds to three layers in the (111) direction. All metals are modeled in fcc stacking. A vacuum region of 15 Å perpendicular to the surface separates the slab from its periodic images and a dipole correction is applied.[36] During the relaxation, the bottom six metal layers are fixed in their bulk-truncated positions, while the top three layers and the adsorbate are relaxed until the maximum force on each atom fell below 0.05 eV/Å. For the calculation of diffusion

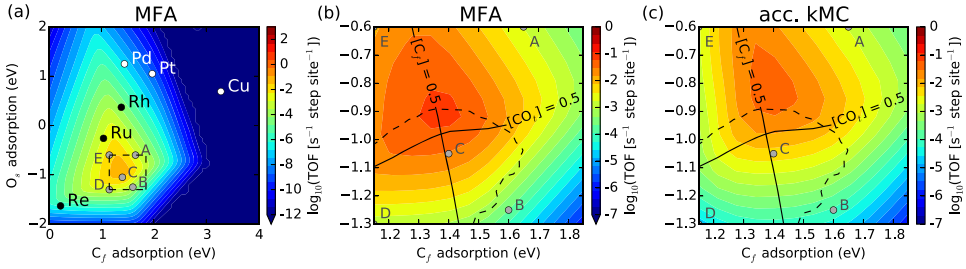

FIG. 3. Theoretical activity maps (volcano plots) for the formation of CH_4 as a function of the C_f and O_s adsorption energies. The indications of special descriptor points and the reaction conditions are as in Fig. 2. The map in (b) is a zoom of the region marked with a dashed line in (a) calculated in the MFA, while the map in (c) is the corresponding region calculated from the modified implementation of accelerated kMC, using explicitly DFT-calculated C and CH diffusion barriers and for a value of N_f equal to the number of unit cells in the simulation box. In (b) and (c), the solid lines indicate the contour line where the coverage of C on the *f* site (vertical line) or the coverage of CO on the *t* site (horizontal line) is equal to 0.5, while the dashed line indicates the contour line where the degree of rate control for the O_s hydrogenation step is equal to 0.08 as calculated in the MFA (cf. Figs. 2 and 4), see text.

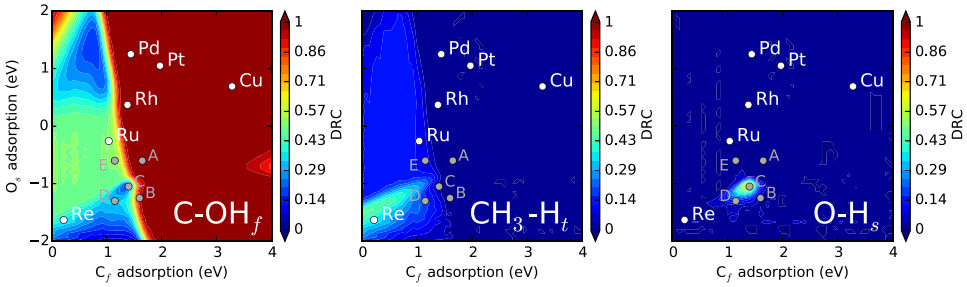

FIG. 4. MFA degree of rate control maps for the C–OH$_f$, CH$_3$–H$_t$, and O–H$_s$ TSs as a function of the C$_f$ and O$_s$ adsorption energies. The indications of special descriptor points and the reaction conditions are as in Fig. 2.

barriers for C and CH, we increase the number of layers in the slab to twelve, with the bottom six layers kept fixed while the top six layers and the adsorbate are relaxed. This is necessary since the very strong interaction of C with some metals at the *f* site leads to significant displacements of the metal atoms in the surface layers in the nudged elastic band (NEB) images along the diffusion pathway. In contrast, a comparison of the adsorption energies for C at the *f* site and CH at the *f* and *t* sites calculated using nine-layer slabs (cf. Table S1 in Sec. S3 of the supplementary material) and using twelve-layer slabs (cf. Table S2 in Sec. S3 of the supplementary material) shows that the average change in adsorption energy when increasing the number of metal layers from nine to twelve layers is below 50 meV. For all calculations, the Brillouin zone is sampled with a (4 × 4) **k**-point grid and cutoffs of 500 eV and 5000 eV are used for the orbitals and the charge density, respectively.

The (1 × 2) supercell used for all calculations is illustrated in Fig. 1 along with the sites used for the different adsorbates. For each combination of adsorbate, metal, and generic site (*s* or *t*), adsorption energies on all of the high-symmetry sites (ontop, bridge, and hollow) were calculated, and the site with the lowest energy is used in the kinetic simulations. Transition-state (TS) energies are calculated using either the climbing-image NEB (CI-NEB) method[37] or the fixed bond length (FBL) method. The harmonic vibrational frequencies of the adsorbates (including the TSs) are calculated on Rh(211) using the Atomic Simulation Environment (ASE) code.[38] It is assumed that the frequencies are constant along the TM series. In computing the free energies of the adsorbates, imaginary and low frequency modes below a cutoff value of 6.9 meV are set to the cutoff value to approximate the entropy contribution from a pseudotranslational/rotational degree of freedom, as discussed in Refs. 13 and 39. Free energy corrections are calculated both for the adsorbates (in the harmonic approximation) and for the gas-phase species (in the ideal gas approximation) using the ASE thermochemistry module. For the gas-phase species, the DFT-calculated energy is used along with experimental vibrational frequencies.[40] All energies and vibrational frequencies are listed in Sec. S3 of the supplementary material, and all structures are provided as XYZ files, also in the supplementary material.

D. Kinetic Monte Carlo simulations

The kMC method relies on coarse-graining of the system dynamics to consider only the rare events representing adsorption, desorption, diffusion, and reaction. Assuming that the system has equilibrated between any two rare events, and thereby lost any memory of the previous state, leads to the Markovian master equation[16–19]

$$\frac{dP_I(t)}{dt} = -\sum_{J\neq I} k_{IJ}P_I(t) + \sum_{J\neq I} k_{JI}P_J(t), \tag{6}$$

where the sum runs over all states J accessible to the system, $P_I(t)$ is the probability to find the system in state I at time t, and k_{IJ} is the rate constant (cf. Sec. II A) or probability for the system to jump from state I to state J. During a kMC simulation, the system is propagated from state to state using a sequence of random numbers and the rates of the possible processes in each state in order to generate trajectories in time. Averaging over infinitely many trajectories yields the evolution of the probability density representing the system kinetics. Thereby, a numerical solution to the master equation is achieved, which allows to fully account for the detailed spatial distribution of the reaction intermediates at any time.

The kMC simulations are performed using the kmos software package,[30] which is based on the rejection-free variable step-size method. As in the MFA study from Ref. 7, the kMC unit cell that is used contains a terrace consisting of a single *s* site, *t* site, and *f* site (cf. Fig. 1). In principle, both the MFA and kMC models could be extended to consider wider terraces by elongating the unit cell with additional *t* sites. However, steps taking place on all three site types are found to exert a large degree of rate control (DRC) over the dominant pathway (*vide infra*) so that adding only additional *t* sites is unlikely to qualitatively change the results. A simulation box is used containing one unit cell in the direction perpendicular to the step and 20 unit cells in the direction parallel to the step, unless otherwise stated in the text. We found that the results are independent of the number of unit cells in the direction perpendicular to the step, i.e., a box with a width corresponding to a single step is sufficient. It was also verified that the use of larger simulation cells in the parallel direction does not affect the results obtained. Periodic boundary conditions are employed both perpendicular and parallel to the step.

Each kMC data point presented in Figs. 5 and 6 corresponds to the average of 24 simulations, differing from each other only in the sequence of random numbers used. Each of these simulation is first run until a steady state is achieved, assessed by the temporal convergence of coverages and turnover-frequencies (TOFs). We note that this could require up to 10^{11} kMC steps for the most expensive calculations. In order to accelerate the convergence to the steady state, the

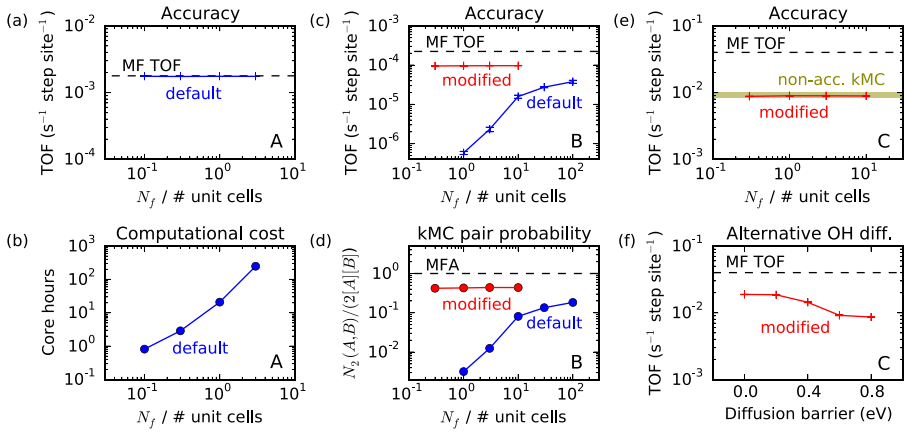

FIG. 5. kMC results for point *A* showing (a) the TOF and (b) the computational cost as a function of the equilibration factor divided by the number of unit cells in the simulation box (N_f/# unit cells). kMC results for point *B* showing (c) the TOF and (d) the ratio between the kMC probability to find an OH species at an *s* site next to OH at a *t* site ($N_2(A, B)$) and the MF-estimated value ($2[A][B]$) again as a function of N_f/# unit cells. kMC results for point *C* showing (e) the TOF as a function of N_f/# unit cells and (f) the TOF as a function of the diffusion barrier for the added alternative OH diffusion pathway (see text). The default (modified) implementation of the algorithm is plotted in blue (red) and non-accelerated kMC results are plotted in yellow (see text).

simulations are always initiated from a surface coverage corresponding to the MFA solution (*vide infra*). Once a simulation reaches steady-state, we begin the *production run* which runs until 250 CH_4 molecules have been produced. The reported turn-over-frequencies (TOFs) are averages over these production runs. The resulting error bars are in most cases too small to be visible in the plots. For the non-accelerated kMC runs, it was not possible to run the simulation long enough to obtain production runs producing 250 CH_4 molecules. Instead, these runs only produced 10–80 produced CH_4 molecules. The resulting error bars are indicated either directly or by the shaded area in Figs. 5 and 6. The kMC results presented in Fig. 3(c) are based on a single trajectory for each descriptor point, producing at least 500 CH_4 molecules in the production run.

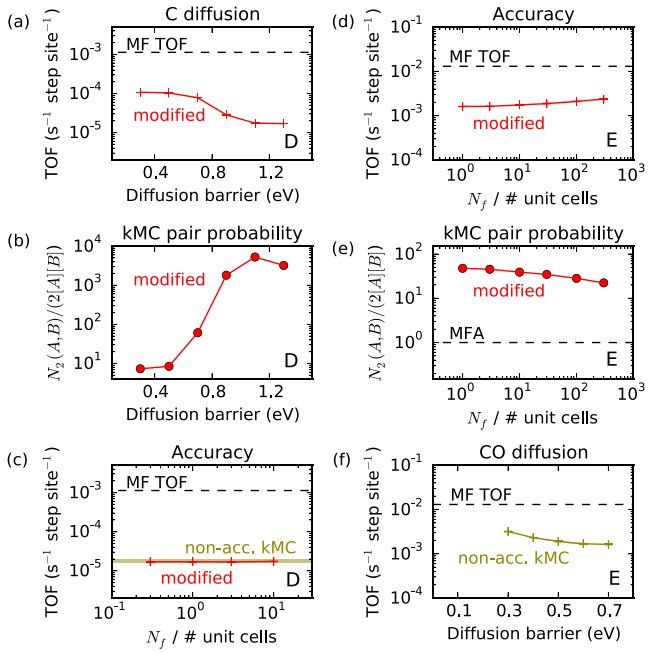

FIG. 6. kMC results for point *D* showing (a) the TOF and (b) the ratio between the kMC probability to find a CH species at a *t* site next to a vacancy at an *f* site ($N_2(A, B)$) and the MFA-estimated value ($2[A][B]$) as a function of the barrier for C *f* to *f* site diffusion. In (c) we show the kMC TOF as a function of N_f/# unit cells for the model with DFT-calculated diffusion barriers (see text). kMC results for point *E* showing (d) the TOF and (e) the same kMC pair probability as in (b) as a function of N_f/# unit cells. In (f) is shown the non-accelerated kMC TOF as a function of the barrier for CO diffusion on the *s* and *t* sites. Note that the results in (a) and (b) have been obtained using a simulation box containing 200 lattice sites parallel to the step (see text).

As already discussed in Sec. I, a major efficiency bottleneck for kMC simulations on metals is the presence of processes that occur on very different time scales. In order to overcome this time scale disparity problem, we employ a twofold strategy: (i) we treat the adsorption, desorption, and diffusion of H on the *h* site in a MFA ansatz (cf. Sec. S4 of the supplementary material) and (ii) we implement and test a recently developed algorithm[29] for achieving temporal acceleration of kMC simulations in the kmos code. A brief overview of the algorithm and its parameters is presented next. Further details can be found in Ref. 29.

E. Acceleration algorithm

The acceleration algorithm of Dybeck, Plaisance, and Neurock[29] pairs all processes in the reaction model into a forward and a reverse process belonging to a given reaction channel, *m*. In our default implementation of the algorithm within kmos, a reaction channel is defined by the type of the process and the site(s) on which it occurs. This means that, e.g., CO adsorption/desorption on the *s* and *t* sites are considered as separate reaction channels. This is necessary since the binding energy of CO differs between these sites, making these reaction channels execute on different time scales. In a modified implementation of the algorithm, we altered the definition of the reaction channels for selected processes to also include the occupation of sites neighboring the site on which the process takes place (*vide infra*). For diffusion processes, the reverse process is defined as diffusion in the opposite direction.

During the kMC simulation, all reaction channels are dynamically partitioned into quasi-equilibrated and non-equilibrated sets. The criteria for a reaction channel m to be labeled as quasi-equilibrated is

$$\frac{|n_{m,\text{forward}} - n_{m,\text{reverse}}|}{n_e} \leq \delta, \tag{7}$$

where $n_{m,\text{forward}}$ and $n_{m,\text{reverse}}$ are the number of forward and reverse executions of reaction channel m, and δ is an adjustable parameter that determined the cutoff between quasi-equilibrated and non-equilibrated reaction channels. The number of forward and reverse executions of each reaction channel is tracked over the last n_e total executions of that reaction channel in either the forward or reverse direction, where n_e is also an adjustable parameter. We use the default values of $\delta = 0.2$ and $n_e = 200$ proposed in Ref. 29, which appear to give an optimal balance between accuracy and efficiency for our reaction model as well. At the start of the simulation, all reaction channels are flagged as non-equilibrated. During the kMC simulation, this status is then continually updated for all reaction channels that have executed more than n_e times.

Once a reaction channel has been flagged as quasi-equilibrated, it can be subject to scaling. The scaling is carried out by decreasing the rate constant of both the forward and the reverse process of a quasi-equilibrated reaction channel by multiplication with a scaling factor $0 < \alpha_m < 1$,

$$k_i' = \alpha_m k_i, \tag{8}$$

where k_i' is the scaled and k_i is the non-scaled rate constant of process i belonging to reaction channel m. The same scaling factor is always applied to the forward and reverse process of each reaction channel in order to preserve the underlying thermodynamics (i.e., detailed balance).

The scaling approach is based on the concept of a *superbasin*, which is defined as the set of all configurations that are accessible to the system by only executing quasi-equilibrated processes. In contrast, the execution of a non-equilibrated process takes the system to a new superbasin. Effectively, the scaling of the rate constants of fast quasi-equilibrated processes encourages the system to leave the superbasin sooner than would be the case in a non-accelerated simulation. The value of the scaling factor α_m is determined in order to allow for an average of N_f executions of either the forward or the reverse process in reaction channel m before the systems exits the current superbasin. The resulting scaling factor is given by

$$\alpha_m = N_f \frac{2r_S}{r_{m,S} + r_{-m,S}}, \tag{9}$$

where N_f is an adjustable parameter referred to as the equilibration factor, which determines how aggressively the quasi-equilibrated processes are scaled, and r_S is the effective rate for escaping from the explored region of the current superbasin, defined as

$$r_S = \sum_{m \in N, Q_B} r_{m,S}. \tag{10}$$

Here, N denotes the set of all non-equilibrated reaction channels and Q_B denotes the set of all reaction channels that have not yet been sufficiently executed to be considered locally equilibrated. A reaction channel is considered locally equilibrated when it has executed a total number of n_e times in either the forward or the reverse direction within the current superbasin. The quantities $r_{m,S}$ and $r_{-m,S}$ in Eqs. (9) and (10) are the rates of the forward and reverse directions of reaction channel m averaged over the time spent in the current superbasin. The scaling factors α_m are readjusted at intervals of N_S kMC steps, where N_S is an adjustable parameter. The value of this parameter does not appear to be important for either the accuracy or the efficiency of the algorithm. We used a value of $N_S = 20$.

Once a non-equilibrated process is executed, all scaling factors are reset to unity and all reaction channels are flagged as *not locally equilibrated*, while the division into quasi-equilibrated and non-equilibrated reaction channels is not affected. The system then enters a new superbasin and the scaling process is restarted. Further details concerning the superbasin concept and the associated terminology can be found in Refs. 28 and 29.

In practice, we fix three of the adjustable parameters (n_e, δ, and N_S) to their default values, while the accuracy of the algorithm is tested by varying the N_f parameter. Note that when N_f goes to infinity, no scaling of the rate constants is carried out, and the accelerated kMC simulation reduces to a non-accelerated simulation. The required value of N_f was found to be related to the system size; we therefore present the results as a function of N_f divided by the number of unit cells in the simulation box. When N_f is equal to the number of unit cells, the quasi-equilibrated processes execute on average once per site in the simulation box before the execution of a non-equilibrated process. We consider the algorithm to be accurate when the results are converged at this value of N_f.

During the testing of the algorithm, we realized that the efficiency could be substantially improved by considering all diffusion processes to be equilibrated (but not locally equilibrated) by default. This means that the execution of a diffusion process will never cause the system to exit the current superbasin and the scaling factors to be reset. In the beginning of the simulation, such resets could substantially reduce the efficiency of the algorithm. However, diffusion processes still need to execute at least n_e times within the superbasin before being labeled as locally equilibrated and being subject to scaling.

F. Mean-field microkinetic model

In the MFA, the detailed spatial configuration of the reaction intermediates is coarse-grained into a mean coverage. Thereby, spatial correlations in the positions of the reaction intermediates and fluctuations away from the mean coverage, both of which are correctly described in kMC simulations, are neglected. In the MFA microkinetic model, the rates $r_{\text{IS}\to\text{FS}}$ for the elementary processes take the form

$$r_{\text{IS}\to\text{FS}}(T, p_i) = N_{\text{IS}}^{\text{FS}} k_{\text{IS}\to\text{FS}}(T, p_i) \prod_{\Theta_i \in \Theta_{\text{IS}}} \Theta_i, \tag{11}$$

where $N_{\text{IS}}^{\text{FS}}$ is a geometric factor accounting for the connectivity of the sites involved in the initial and final states of the

process. The rate constants, $k_{IS\rightarrow FS}$, are given in Sec. II A, and Θ_i is the coverage of species i belonging to the IS. The sum of all coverages for each type of adsorption site (t, s, and f) is constrained to 1. The resulting set of coupled differential equations is solved to determine the coverages and rates at steady state using the CatMAP software package.[41] CatMAP uses a modified multidimensional Newton's method root-finding algorithm, which is iterated until the rate of change for all coverages is below 10^{-50}. The time scale disparity problem is also present in the MFA model as an extreme stiffness of the differential equations, which requires the use of multiple precision up to 100 digits.

Both the MFA and kMC results are presented for conditions typical of reactor operation (T = 523 K and p = 1 bar with a gas composition of 1% CO, 97% H_2, 1% CH_4 and 1% H_2O) as has also been employed in Ref. 7.

III. RESULTS AND DISCUSSION

A. Mean-field results

Figure 2 shows the steady-state coverages of the surface species CO, O, OH, and C as a function of the C_f and O_s adsorption energies, as obtained by the MFA model. CO and O both adsorb at the s and t sites and thus compete for coverage at these sites. As the oxygen adsorption energies on these sites become more negative compared to the carbon adsorption energy, the dominant adsorbate on these sites switches from CO to O. This transition occurs at a more negative value of the oxygen adsorption energy (at fixed carbon adsorption energy) on the t sites compared to the s sites. This can be explained from the DFT adsorption energies (cf. Sec. S3 of the supplementary material) in which O binds stronger relative to CO by a greater amount on the s site than on the t site. The coverage of OH is negligible on the t site (not shown), whereas high OH coverage is present on the s site in a small area at weak C_f adsorption energies and intermediate O_s adsorption energies (cf. Fig. 2). Adsorption of atomic carbon is most favorable at the f site and is present on this site at high coverage for strong C_f adsorption energies (shown), whereas the C coverages on the s and t sites are negligible (not shown). The coverages of CH, CH_2, and CH_3 at all sites are negligible (not shown).

As expected, the metals that are known to interact very strongly with O and C (e.g., Re) show high surface coverages of these two species. This could lead to surface morphological changes such as the formation of oxides or carbides.[19,42–44] Further, the very high coverages predicted on many of the metals could also lead to sizable lateral interactions between the adsorbates.[14,15,45] The description of these effects and their impact on catalyst activities is, however, outside of the scope of the present work.

The TOF map (volcano plot) for CH_4 formation is shown in Fig. 3(a). Our results can be compared to Fig. S3(c) from the supplementary material of Ref. 7, which contain neither the direct effect of lateral interactions nor the indirect effect of using a scaling relation for CO dissociation calculated for high CO coverages. This comparison shows that the position and absolute TOF of the volcano maximum agree reasonably well with this previous study, while the overall shapes of the volcanoes differ significantly. These differences could be caused either by the different approximations at the level of the DFT calculations used in the two studies (the RPBE functional and the Dacapo DFT code was used in Ref. 7) or by the more extended reaction model considered in the present study.

Under the present consideration of an extended reaction model, it is also possible to use the MFA solution to reveal the dominant reaction pathway at each descriptor point. This is important for the analysis of the kMC results in Sec. III B since the MFA and kMC models follow the same dominant reaction pathway. The steps in this pathway are characterized by the fact that the net rate (the forward minus the reverse rate) is nearly equal to the overall TOF, while unimportant reaction steps typically have net rates that are orders of magnitude lower than the TOF. The dominant reaction pathway identified this way turns out to be rather constant in most of descriptor space (at least around the points A–E in Fig. 3(a) which are used as test cases for the kMC simulations) and is characterized by the following steps:

1. $CO(g) + *_t \rightleftharpoons CO_t$,
2. $H_2(g) + 2\,*_h \rightleftharpoons 2\,H_h$,
3. $CO_t + H_h + *_f \rightleftharpoons OH_t + *_h + C_f$,
4. $C_f + H_h \rightleftharpoons CH_f + *_h$,
5. $CH_f + *_t \rightleftharpoons *_f + CH_t$,
6. $CH_t + H_h \rightleftharpoons CH_{2t} + *_h$,
7. $CH_{2t} + H_h \rightleftharpoons CH_{3t} + *_h$,
8. $CH_{3t} + H_h \rightleftharpoons *_t + *_h + CH_4(g)$,
9. $O_s + H_h \rightleftharpoons OH_s + *_h$,
10. $OH_s + OH_t \rightleftharpoons H_2O(g) + O_s + *_t$.

It should be noted that several of these steps were not considered in the MFA model of Lausche *et al.*,[7] i.e., they considered only the most stable s adsorption site for CO and OH, while we find that the t adsorption site is actually involved in the dominant reaction mechanism.

Equally important is an analysis of the rate-determining steps of the dominant reaction pathway at each descriptor point. Figure 4 shows the degree of rate control (DRC) maps for selected elementary steps calculated using the method described in Ref. 46, where a DRC value larger than zero signifies a partly (DRC smaller than one) or completely (DRC equal to one) rate-determining step. As expected, CO dissociation (occurring through TS C–OH_f) is the rate-determining step in most of the descriptor space, in particular for weak C_f adsorption which through the scaling relations translates into weak adsorption of the reactants in this step, CO and H. This is the only rate-determining step for point A. At stronger O_s adsorption (points B, C, and D), an elementary step involved in the water formation pathway, the hydrogenation of O at the s site, becomes partly rate-limiting as well. Finally, at stronger C_f adsorption (points D and E), the hydrogenation of CH_3 at the t site also becomes partly rate-limiting. The barriers for the diffusion processes between different site types are not rate-limiting; thus, no refinement of the diffusion barriers was judged necessary for the MFA model.

B. Kinetic Monte Carlo results

The testing of the kMC acceleration algorithm was carried out at five points (*A*, *B*, *C*, *D*, and *E*) around the maximum of the MFA volcano plot (cf. Fig. 3(a)). As described above, each of these points is characterized by significantly different rate-limiting steps and surface coverages (cf. Figs. 2 and 4), and thus they provide a diverse set of test scenarios for the algorithm. For the diffusion barriers, the approximate values discussed in Sec. II A are used as an initial estimation. Whenever the results were found to be sensitive to the exact value of a diffusion barrier, that barrier was refined through explicit DFT calculations.

We first consider the point *A*, which is characterized by high coverages of CO on the *s* and *t* sites, with vacant *f* sites. The rate-determining step at this point is the dissociation of CO. The kMC TOF for point *A* is plotted in Fig. 5(a) as a function of the equilibration factor N_f divided by the number of unit cells in the simulation box. The processes that get scaled by the algorithm are CO adsorption/desorption at the *s* and *t* sites, all CO, O, and OH diffusion processes, steps 9 and 10 related to the dominant water formation pathway, C diffusion between *f* sites, nearly all CH diffusion steps, and steps 4-6 related to C and CH_x hydrogenation. It is seen that the kMC TOF is equal to the MFA TOF and that the results are insensitive to the value of N_f. Similar to the MFA results, the kMC results at point *A* are found to be insensitive to the exact value of the diffusion barriers of all reaction intermediates (not shown).

The computational cost of the simulation for point *A* is plotted as a function of N_f in Fig. 5(b). It is seen that the cost grows roughly linearly with the N_f parameter. The exact value of the speedup compared to non-accelerated kMC cannot be measured directly due to the exceeding computational cost of the latter simulation. However, at point *A* the rate of the slowest process (CO dissociation) can be estimated to be around 10^{-3} s^{-1}, while the (non-accelerated) rate of the fastest process (CO diffusion on the *t* site) can be estimated to be around 10^{10} s^{-1}. In a non-accelerated simulation, CO diffusion would thus be expected to execute around 10^{13} times for each CO dissociation event. For N_f equal to the number of unit cells in the simulation box, it is found that an average of 10^7 kMC steps are needed to execute one CO dissociation step. We thus estimate the speedup to be around six orders of magnitude. Thus, the algorithm works well and the computational speedup is indeed significant. In that regard, it is worth mentioning that our implementation of the acceleration algorithm in kmos results in an increase in computational cost per kMC step of only about 10% compared to non-accelerated kMC. This is negligible compared to the speedup achieved by the acceleration algorithm.

Next, we consider point *B*, where the *s* and *t* sites are covered by O, while the *f* site is vacant. In addition to CO dissociation, the hydrogenation of O at the *s* site is also partly rate-limiting at point *B*. In Fig. 5(c) we plot the kMC TOF as a function of N_f for the default implementation of the algorithm (blue points) as well as for a modified implementation of the algorithm (red points, *vide infra*). The processes that get scaled are similar to the ones listed for point *A*, with the important exception of OH diffusion. In fact, as a consequence of the much lower coverage of *t* and *s* vacancies at point *B* compared to point *A*, the surface diffusion of OH is almost completely suppressed at point *B*. For the default implementation of the algorithm, the convergence with respect to N_f is very slow and the results are far from being converged when the equilibration factor equals the number of unit cells in the simulation box. To understand this breakdown of the algorithm, we plot in Fig. 5(d) the kMC probability to find an OH species at an *s* site next to OH at a *t* site (as required for step 10, the dominant water formation pathway), scaled by the MFA probability to form the two neighboring OH groups (the product of the site-connectivity factor 2 for *s* and *t* sites and the kMC surface coverages of OH_s and OH_t). We can see that the kMC probability is much lower than the MF probability—in fact, the deviation is nearly identical to the deviation of the kMC TOF from the MFA TOF (cf. Fig. 5(b)). Therefore, it appears that the poor convergence of the accelerated kMC results with respect to N_f is related to this probability being artificially decreased by the acceleration algorithm.

This problem arises because the acceleration algorithm scales the rate constant for OH formation at the *s* and *t* sites too aggressively to allow for sufficient sampling of configurations containing pairs of adjacent OH_s and OH_t species. This issue is actually quite general and can occur whenever a pair of independent (i.e., not sharing any reactant/product species) quasi-equilibrated thermodynamically unfavorable processes (steps (a) and (b)) must occur sequentially in order to form a pair of adjacent species A and B (OH_s and OH_t in this case), which then react with each other in a third step (c),

(a) $\ldots \rightleftharpoons \mathrm{A} + \ldots,$
(b) $\ldots \rightleftharpoons \mathrm{B} + \ldots,$
(c) $\mathrm{A} + \mathrm{B} \rightleftharpoons \ldots.$

In Sec. S5 in the supplementary material, we further analyze this case and show that adequate sampling of configurations containing pairs of adjacent OH_s and OH_t species requires a value of N_f that is sufficiently greater than $\min(K_a^{-1}, K_b^{-1})$, where K_a and K_b are the equilibrium constants of steps (a) and (b), respectively. At point *B* the value of K_a (K_b) is around 10^{-3} (10^{-10}). Therefore, the value of N_f should be sufficiently greater than $\sim 10^3$, which is a much larger value than the criteria we defined for the acceleration algorithm to be accurate for non-problematic systems (N_f equal to the number of unit cells in the simulation box as discussed in Sec. II E) and is in between the two largest N_f values considered in Fig. 5(c).

The criteria for N_f we defined in Sec. II E was based on the assumption that step (a) (or step (b)) must execute an average of once per site in the simulation box before exiting the current superbasin, in order for the acceleration algorithm to be accurate. However, this is not a sufficient criterion for this type of reaction scheme. Step (a) (or step (b)) must instead execute a sufficient number of times (i.e., many more than once) on a site next to species B (A) generated by step (b) (step (a)) before the system exits the current superbasin. When both K_a and K_b are unfavorable for the forward reactions, most of the executions of step (a) (step (b)) will occur in the absence of an

adjacent species B (A). As a result, an insufficient number of adjacent A/B pairs will form within the residence time of the current superbasin when using an N_f value equal to the number of unit cells in the simulation box. For N_f values lower than ten times the number of unit cells in the simulation box, step 10 is in fact not executed at all, while for higher values it is executed insufficiently. Instead, the alternative water formation pathway relying on the direct hydrogenation of OH at the *s* site (Eq. (S17) in the supplementary material) is selected for escaping the current superbasin. Typically, we can expect the correct sampling of a highly improbable surface configuration not to be important for the correct evolution of the system. However, in this particular case the water formation pathway relying on the reaction of two neighboring low-coverage OH adsorbates is an important step in the mechanism. It is preferred over the direct hydrogenation of OH at the *s* site since the latter process has a much lower rate constant ($k_{\mathrm{H-OH}_s} = 10^{-4}\ \mathrm{s}^{-1}$) than the former ($k_{\mathrm{OH}_s-\mathrm{OH}_t} = 3 \times 10^{11}\ \mathrm{s}^{-1}$).

One way to correct this poor performance of the acceleration algorithm is to scale the rate constants of steps (a) and (b) differently when they occur on a site next to a species of B or A, respectively. This entails modifying the assignment of events to reaction channels. Instead of assigning every O hydrogenation event on, e.g., the *t* site to the same reaction channel, we distinguish between the different possibilities for the occupation of the two neighboring *s* sites. This means that the hydrogenation of O occurring in a configuration with, e.g., O atoms on the two neighboring *s* sites belongs to a different reaction channel (and thus gets scaled differently) from the hydrogenation of O occurring in a configuration where, e.g., one of the neighboring *s* sites is occupied by OH. Similarly, the O hydrogenation on the *s* site is assigned to different reaction channels depending on the occupation of the two neighboring *t* sites. This ensures that whenever the formation of two neighboring OH groups is possible, the required O hydrogenation process can execute with the non-scaled rate constant (since this process has likely never occurred before within the current superbasin). We note that this modification effectively represents a step on the way towards the algorithm proposed by Chatterjee and Voter,[28] where a process is defined by the configuration of the entire system and not just by the configuration of the nearest neighbors. However, the inclusion of nearest neighbor configurations as performed here already increases the total number of reaction channels significantly. This, in turn, decreases the efficiency of the acceleration algorithm. The approach pursued here therefore represents an attempt to find an optimum between the accuracy and efficiency of acceleration algorithms.

The results obtained using the modified implementation are shown with red points in Figs. 5(c) and 5(d). The kMC TOF is now insensitive to the value of N_f, i.e., the algorithm works well. However, the MFA TOF is still not recovered in this case, which is reflected by the fact that the kMC probability to find an OH species at an *s* site next to an OH species at a *t* site stays below the MFA-estimated value. This difference can be traced to the fact that OH diffusion is completely suppressed as a consequence of the low OH and vacancy coverage on the *s* and *t* sites. The remaining difference in TOF between MFA and kMC is thus not an artifact of the acceleration algorithm, but a breakdown of the MFA itself.

We further investigate this breakdown of the MFA for the point *C*, which is located at the descriptor point where the TOF is maximally sensitive to the rate of water formation through the rate-limiting step of OH formation on the *s* site (cf. Fig. 4) and where correspondingly the largest difference between the MFA and kMC TOF is observed. Since the rate of CO diffusion is very low at point *C* (as a consequence of low CO and vacancy coverage on the *s* and *t* sites), while the rate of the rate-limiting step is sufficiently high (as a consequence of the proximity to the top of the volcano), the time scale disparity at point *C* is small enough to allow for comparison with non-accelerated kMC simulations. In Fig. 5(e), we plot the kMC TOF for point *C* as a function of N_f both with and without the acceleration scheme. The results confirm that the acceleration algorithm works properly and that the MFA also breaks down for this point. The kMC results are found to be insensitive to the barriers for diffusion of all reaction intermediates, including OH (not shown), since OH diffusion is not limited by its rate constant, but by the low coverage of vacancies on the *s* and *t* sites.

While the MFA is found to break down for the presently considered reaction mechanism, it is possible that other diffusion mechanisms that are not included in our model could affect the diffusion of OH groups on the surface. Such an alternative diffusion pathway could be the transfer of the H atom in the OH group to a neighboring O atom, which has been found to occur with a barrier of around 0.5 eV on rutile $TiO_2(110)$.[47] In Fig. 5(f), we include this diffusion process parallel to the step (i.e., from *t* to *t* site and from *s* to *s* site) and plot the kMC TOF as a function of the corresponding barrier for diffusion. The kMC TOF indeed increases for very small barriers of such alternative OH diffusion mechanism. It should be noted that if H transfer between O_s and O_t species is also included in the reaction model, the mechanism for water formation changes, as evidenced by a change in the rate-determining step and TOF for the MFA model (not shown). Since overall the observed changes when including such alternative OH diffusion pathways are relatively minor and limited to the small area of descriptor space where the hydrogenation of O_s is rate-limiting, we do not calculate the barriers for these processes using DFT.

Next, we move to the point *D*, which differs from points *B* and *C* in the high coverage of C on the *f* site and the fact that CH_3 hydrogenation on the *t* site is partly rate-limiting as well. At point *D*, we find that the kMC TOF is particularly sensitive to the barrier for C diffusion between *f* sites, as shown in Fig. 6(a). For very low C diffusion barriers, we furthermore find that the kMC TOF is strongly dependent on the length of the simulation box parallel to the step and increases linearly for small step lengths. The kMC results presented in Fig. 6(a) therefore had to be carried out using a significantly larger simulation box of 200 lattice sites parallel to the step. These finite-size effects are further discussed in Sec. S6 of the supplementary material.

To understand why the kMC TOF is sensitive to the C diffusion barrier at point *D*, consider that the rate of CH_4 formation is proportional to the concentration of CH_x species

on t sites. These species are formed by step 5 in the reaction mechanism, whereby a CH diffuses from an f to a t site. Their steady-state concentration is therefore determined by the relative rates of the forward and reverse directions of this step (since CH_4 formation is negligibly slow compared to this step). The reverse rate of step 5 is proportional to the concentration of CH_t species that are adjacent to f vacancies. Such configurations are formed by step 5 and broken up by diffusion of the CH_t or the f vacancy, the latter occurring via C diffusion. When these latter processes are limited by low rates of CH and C diffusion, the reverse rate of step 5 is higher, and as a result, the concentration of CH_{xt} species and the rate of CH_4 formation are reduced.

We can see that this is the case by examining Fig. 6(b), in which we plot the kMC probability to find a CH on a t site adjacent to a vacancy on a f site, normalized by the MFA-estimated probability for this configuration (when either C_f or CH_t diffusion is infinitely fast, this quantity will be unity). The results show that for high C diffusion barriers, diffusion is too slow to break up the configurations containing adjacent CH_t and f vacancies (at this descriptor point, CH_t diffusion is too slow to be significant), which is reflected by a significantly increased kMC probability to sample this configuration. This leads to an increased rate of CH diffusion back to the f site and a reduction in the CH_{xt} concentration and the rate of CH_4 formation.

The effect just described is observed for any descriptor point with a high coverage of C on the f site. Since the effect on the TOF is substantial and since a high C coverage is found in a relatively large area of descriptor space, we explicitly calculated the important diffusion barriers using DFT. These include CH diffusion between f and t sites, which determines the rate of step 5 in the reaction mechanism, as well as C diffusion between two f sites and CH diffusion between two t sites, which in turn determines the likelihood of CH_t and $*_f$ to diffuse away from each other after being formed in step 5.

The DFT results for C diffusion on Ru(211) are presented in Fig. 7. Surprisingly, the direct f to f site diffusion pathway has an extremely high barrier of around 1.6 eV. Considering the structures for the initial state (*A* in Fig. 7) and the TS (*B* in Fig. 7), the high barrier seems to be related to the fact that the C atom has to move from a very favorable position, buried down in the metal surface and coordinated to four Ru atoms (*A*), to a highly unfavorable position in which it is coordinated to only two Ru atoms (*B*). In an alternative diffusion pathway, the C atom diffuses via the t site (*D* in Fig. 7), passing through a TS in a terrace bridge position (*C* in Fig. 7). This diffusion pathway has a slightly lower barrier of around 1.3 eV. However, given the extremely low coverage of t vacancies at point *D* at steady state, this pathway is not feasible and is in fact never observed in the kMC simulations, even when using the originally estimated, much lower, diffusion barrier. The DFT results in Fig. 7 also allow for an estimation of the C t to t site diffusion barrier, which occurs via the TS *C* in Fig. 7. On Ru this barriers is found to be around 0.7 eV, while on Re we find a barrier of around 0.5 eV. The latter barrier corresponds well to the value estimated for t to t site diffusion on Re(0001) (also 0.5 eV) in Ref. 10. The energies and vibrational

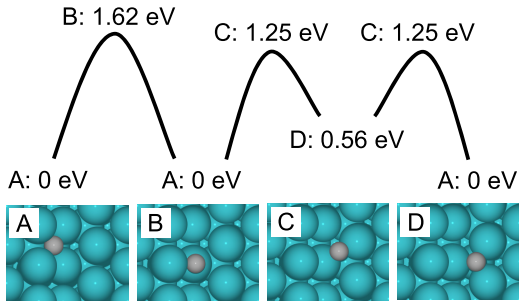

FIG. 7. DFT structures and adsorption energies for different C diffusion pathways on Ru(211). All energies are given with respect to the most stable adsorption site of C at the f site (structure *A*). Structure *B* shows the TS for the direct f to f site diffusion pathway, while structure *C* shows the TS for the f to t site or t to t site diffusion pathway. Structure *D* shows the most stable adsorption site at the t site.

frequencies related to C and CH diffusion on all metals are listed in Sec. S3 of the supplementary material, while the scaling plots and fitted scaling parameters can be found in Sec. S2 in the supplementary material.

Using the explicitly calculated DFT barriers for C and CH diffusion, we plot in Fig. 6(c) the kMC TOF as a function of N_f for point *D*. The processes that get scaled by the algorithm at point *D* are similar to those at points *B* and *C* except that, with the explicitly calculated C diffusion barrier, this process is now too slow to actually get scaled. The value for the C diffusion barrier at point *D* is found to be around 1.5 eV, which results in an almost complete suppression of C diffusion. CH diffusion between t sites is also found to be almost completely suppressed, but in this case it is predominantly a result of the low coverage of vacancies on the s and t sites. As a result, the kMC TOF is found to be almost two orders of magnitude lower than the MFA TOF at point *D*. This is again a breakdown of the MFA, as the insensitivity to the value of N_f evidences the reliable performance of the acceleration algorithm. This is also confirmed by non-accelerated kMC simulations for this point (cf. Fig. 6(c)).

Finally, we consider the point *E*, which differs from point *D* in the fact that the s and t sites are covered by CO and not O, while the coverage of C on the f site is still high. The rate-limiting steps for this point are CO dissociation and CH_3 hydrogenation. As with point *D*, we use explicitly DFT-calculated C and CH diffusion barriers. The results for the kMC TOF presented in Fig. 6(d) are rather similar to the results for point *D*, except that the kMC TOF at point *E* increases slightly with the N_f value. This increase in TOF is accompanied by a decrease in the kMC probability to sample a CH species on a t site adjacent to a vacancy on an f site, as shown in Fig. 6(e). The processes that get scaled by the algorithm are identical to point *D*, except that OH diffusion additionally gets scaled at point *E*. This was also the case for point *A* and is related to the higher concentration of s and t vacancies in a CO-covered surface compared to an O-covered surface. As a consequence of the higher vacancy concentration at point *E*, the diffusion of CH on the t site is also executed more often compared to point *D*. For point *E*, executions are frequent enough that the CH diffusion process between t sites gets scaled slightly by the acceleration algorithm. In contrast, C diffusion continues to be almost completely suppressed at point *E* since it is limited by

the very high C diffusion barrier rather than by the vacancy concentration.

While the slight scaling of the rate constant of the CH t to t diffusion process could potentially affect how effective this process is in breaking up the correlation in position of the CH_t-$*_f$ pair formed in step 5, the CH diffusion could also be affected by the scaling of rate constants for CO diffusion. This is due to the fact that the diffusion of a CH species across a CO-covered terrace proceeds via alternating CH and CO diffusion steps. To further analyze this point, we plot in Fig. 6(f) the non-accelerated kMC TOF as a function of the barrier for CO diffusion on the s and t sites (effectively, what is varied is the BEP offset in the approximate BEP relations used to describe CO diffusion, as discussed in Sec. II A). It is seen that the kMC TOF increases slightly for low barriers of CO diffusion (the lowest barrier that it is computationally feasible to consider for non-accelerated kMC simulations is 0.3 eV, while the barrier estimated for Re in Ref. 10 is 0.11 eV). It therefore seems likely that the slight variations observed in the kMC TOF at large N_f values in Fig. 6(d) are caused by the algorithm artificially slowing down CO diffusion on the t site, which in turn reduces the rate of CH_t diffusion across the terrace. Overall, though, the observed changes in the TOF with N_f (cf. Fig. 6(d)) and with the CO diffusion barrier (cf. Fig. 6(f)) are rather small (at least within the range of parameters that it is computationally feasible to consider). We do not attempt to further refine the barriers for CO diffusion using DFT.

The artificial effect of the acceleration algorithm on the CH_t diffusion rate has a similar cause as the artificial effect on the water formation rate at points B and C. CH_f formation followed by diffusion to a t site and t vacancy formation via CO desorption followed by CO diffusion are both quasi-equilibrated thermodynamically unfavorable processes that are independent of one another, corresponding to steps (a) and (b) discussed for the water formation pathway at point B. Likewise, CH_t diffusion proceeds from a configuration containing a CH_t species adjacent to a t vacancy, corresponding to step (c) in that reaction network. The poor convergence of the acceleration algorithm with respect to N_f at point E is therefore likely due to the fact that it reduces the rate of CO diffusion too aggressively for sufficient sampling of configurations containing adjacent $CH_t/*_t$ pairs. Unfortunately, it is not as straightforward to circumvent this problem by modifying the assignment of processes to reaction channels as it was for the water formation pathway due to the complex process by which CH diffuses across a terrace that involves alternating CH and CO diffusion steps. We would anticipate that the algorithm of Chatterjee and Voter[28] would perform better in this case since every unique configuration of $CH_t/*_t$ pairs would represent a separate reaction channel. However, the computational cost of this latter algorithm would most likely be exceedingly high.

To summarize the results of the kMC simulations, we include in Fig. 3 a comparison of the TOF maps calculated using both the MFA and the modified implementation of accelerated kMC (with explicitly DFT-calculated C and CH diffusion barriers and a value of N_f equal to the number of unit cells in the simulation box). In the region near point C where the hydrogenation of O on the s site is rate-limiting in the MF model, small differences are observed. This can be explained by the limited OH diffusion in the kMC model. Larger differences are observed in the regions represented by the points D and E, where the coverage of C species on the f site is high and CH_4 formation on the t site is rate-limiting. This can be explained in terms of the limited diffusion of C between f sites and CH between t sites in the kMC model. Whereas we can confirm by comparison to non-accelerated kMC simulations that the discrepancies between the kMC and MFA results at points C and D are due to a breakdown of the MFA and not poor convergence of the acceleration scheme, we conclude that the discrepancy at point E is likely due to the latter cause. The TOFs in the accelerated kMC model presented in Fig. 3(c) are therefore slightly underestimated in the region of descriptor space that is characterized by high coverage of C on the f site and high coverage of CO on the t site. In reality, the kMC TOF should be closer to the MFA result in these regions. Unfortunately, an accurate estimation of the TOF using non-accelerated kMC is not possible due to the exceeding computational cost of running the simulation with a realistic CO diffusion barrier of around 0.1 eV.

It is worth noting that the MFA ansatz used for describing H in the kMC simulations effectively removes H_2 adsorption/desorption (step 2 in the reaction mechanism) from the kMC model and reduces the hydrogenation/dehydrogenation reactions (steps 4, 6, 7, 8, and 10) to effective first-order reactions. The only second-order reaction steps in the reaction mechanism are therefore steps 3, 5, and 9. The MFA is susceptible to break down for second-order reaction steps where both reactants are present in low coverage.[25] Indeed, reaction steps 5 (low $*_f$ and CH_t coverages) and 9 (low OH_s and OH_t coverages) are found to be responsible for the cases where the MFA is found to break down in this study. Surprisingly, no breakdown of the MFA is observed for step 3 (the reaction of CO_t and $*_f$ to form OH_t and C_f). While a positive correlation between the occupation of an f site by C and the occupation of a neighboring t site by OH (the configuration formed after step 3) is observed at point A, where O species are present in low coverage on the t site and C is present in low coverage on the f site, this does not lead to any visible effect on the TOF, since the rate constant for the reverse of reaction step 3 is so low that this process is negligible. A correlation between the occupation of a t site by CO and a neighboring f site by a vacancy is never observed. One might expect this to occur at point D where the t sites are covered with O and the f sites are covered with C. That no such correlation is observed is probably related to the fact that CO can "diffuse" rather quickly on an O-covered terrace by a three-step process involving CO desorption, diffusion of the resulting vacancy via O diffusion, and CO readsorption on the new vacancy.

IV. CONCLUSIONS

We have implemented a recently developed acceleration algorithm for kMC simulations[29] and tested it using a scaling-relation-based reaction model for CO methanation over stepped transition metal surfaces. While the algorithm

was shown to always be reliable for the simple reaction model tested in Ref. 29, our more thorough testing, using a rather complex reaction model and considering the whole series of TMs, reveals an unforeseen breakdown of the algorithm. The problem occurs when two independent quasi-equilibrated reaction steps produce low-coverage species which then react with each other in a third reaction step. In that case, the acceleration algorithm may scale the rates of the two quasi-equilibrated steps too aggressively for adequate sampling of configurations containing adjacent low-coverage species needed for the third reaction step. Nevertheless, this problem was easily identified by performing proper convergence tests with respect to the N_f parameter, which controls the degree of acceleration that is applied.

In the present case, we were able to correct for the poor performance of the acceleration algorithm in some cases by modifying the way that processes are assigned to reaction channels. This modification was not possible however when the third step was CH diffusion across a terrace due to the complicated mechanism by which this process occurs that involves alternating CH and CO diffusion. This challenging case may therefore serve as a benchmark for future algorithm development. Such development efforts could, for example, aim at finding a better compromise between the algorithm proposed by Chatterjee and Voter,[28] which has (presumably) high accuracy but low efficiency, and the algorithm proposed by Dybeck, Plaisance, and Neurock,[29] which has high efficiency but can give poor accuracy in certain situations.

Regarding the comparison of the MFA and kMC methodologies, our results contradict the widespread assumption that MFA models are always reliable for catalytic reactions on metals in the absence of lateral interactions. For a descriptor point located within a couple of hundreds of meV from the top of the MFA activity volcano (point *D*, cf. Fig. 3), we find that the MFA overestimates the TOF by nearly two orders of magnitude. This could substantially influence the reliability of a screening study attempting to find promising new catalyst materials. We were able to trace this breakdown of the MFA to the fact that diffusion barriers along step sites can be substantially higher than those previously identified along terrace sites[10] since step sites generally bind adsorbates much stronger than terrace sites. This effectively renders stepped-metal surfaces similar to oxide surfaces, where similar breakdowns of the MFA due to high diffusion barriers have been reported before. The presented results demonstrate that kMC models could be used equally well in scaling-relation-based screening studies although the higher accuracy undoubtedly comes at a much higher, yet tractable, computational cost.

The cases where the MFA was found to break down in the present study were all related to slow diffusion in a high-coverage configuration. Of course, it is well known that precisely for these cases the inclusion of lateral interactions could be important for the outcome of the simulation and could significantly influence both the barriers for all processes and the adsorbate coverages. It is possible that the resulting changes could influence the predictions of where the MFA breaks down in the present study. However, it is also well known that the inclusion of interactions could itself lead to a breakdown of the MFA since such interactions tend to lead to the formation of ordered adsorbate structures on the surface, even in cases where all interactions are repulsive.[48] The extension of accelerated kMC methods to models including lateral interactions is therefore an equally important target for future algorithm development.

SUPPLEMENTARY MATERIAL

See supplementary material for additional details about the reaction model, scaling relations, DFT energies, vibrational frequencies and structures, analysis of the accuracy of the acceleration scheme for the water formation pathway, and further kMC results.

ACKNOWLEDGMENTS

M.A. would like to thank the Alexander von Humboldt Foundation for a post-doctoral fellowship. The authors would like to thank Professor Jens K. Nørskov and Professor Andrew James Medford for helpful discussions regarding the MFA microkinetic models. Professor Andrew James Medford, Xinyan Liu, and Devyani Sharma are acknowledged for contributing to the database of DFT calculations used in the present work.

[1] V. Pallassana and M. Neurock, J. Catal. **191**, 301 (2000).
[2] A. Michaelides, Z.-P. Liu, C. J. Zhang, A. Alavi, D. A. King, and P. Hu, J. Am. Chem. Soc. **125**, 3704 (2003).
[3] F. Abild-Pedersen, J. Greeley, F. Studt, J. Rossmeisl, T. R. Munter, P. G. Moses, E. Skulason, T. Bligaard, and J. K. Nørskov, Phys. Rev. Lett. **99**, 016105 (2007).
[4] S. Wang, V. Petzold, V. Tripkovic, J. Kleis, J. G. Howalt, E. Skulason, E. M. Fernandez, B. Hvolbaek, G. Jones, A. Toftelund, H. Falsig, M. Bjorketun, F. Studt, F. Abild-Pedersen, J. Rossmeisl, J. K. Nørskov, and T. Bligaard, Phys. Chem. Chem. Phys. **13**, 20760 (2011).
[5] F. Calle-Vallejo, D. Loffreda, M. T. M. Koper, and P. Sautet, Nat. Chem. **7**, 403 (2015).
[6] S. Dahl, J. Sehested, C. Jacobsen, E. Törnqvist, and I. Chorkendorff, J. Catal. **192**, 391 (2000).
[7] A. C. Lausche, A. J. Medford, T. S. Khan, Y. Xu, T. Bligaard, F. Abild-Pedersen, J. K. Nørskov, and F. Studt, J. Catal. **307**, 275 (2013).
[8] I. A. W. Filot, R. A. van Santen, and E. J. M. Hensen, Angew. Chem., Int. Ed. **53**, 12746 (2014).
[9] M. Andersen, A. J. Medford, J. K. Nørskov, and K. Reuter, Angew. Chem., Int. Ed. **55**, 5210 (2016).
[10] K. Hahn and M. Mavrikakis, Top. Catal. **57**, 54 (2014).
[11] A. Vojvodic, A. J. Medford, F. Studt, F. Abild-Pedersen, T. S. Khan, T. Bligaard, and J. K. Nørskov, Chem. Phys. Lett. **598**, 108 (2014).
[12] L. C. Grabow, B. Hvolbæk, and J. K. Nørskov, Top. Catal. **53**, 298 (2010).
[13] N. Yang, A. J. Medford, X. Liu, F. Studt, T. Bligaard, S. F. Bent, and J. K. Nørskov, J. Am. Chem. Soc. **138**, 3705 (2016).
[14] Y. Zhang, V. Blum, and K. Reuter, Phys. Rev. B **75**, 235406 (2007).
[15] C. Wu, D. Schmidt, C. Wolverton, and W. Schneider, J. Catal. **286**, 88 (2012).
[16] A. Chatterjee and D. G. Vlachos, J. Comput.-Aided Mater. Des. **14**, 253 (2007).
[17] M. Sabbe, M.-F. Reyniers, and K. Reuter, Catal. Sci. Technol. **2**, 2010 (2012).
[18] M. Stamatakis, J. Phys.: Condens. Matter **27**, 013001 (2015).
[19] K. Reuter, Catal. Lett. **146**, 541 (2016).
[20] M. J. Hoffmann and K. Reuter, Top. Catal. **57**, 159 (2014).
[21] J. M. Lorenzi, S. Matera, and K. Reuter, ACS Catal. **6**, 5191 (2016).
[22] S. Piccinin and M. Stamatakis, ACS Catal. **4**, 2143 (2014).
[23] M. Stamatakis and S. Piccinin, ACS Catal. **6**, 2105 (2016).
[24] B. Temel, H. Meskine, K. Reuter, M. Scheffler, and H. Metiu, J. Chem. Phys. **126**, 204711 (2007).

[25]S. Matera, H. Meskine, and K. Reuter, J. Chem. Phys. **134**, 064713 (2011).
[26]E. L. Haseltine and J. B. Rawlings, J. Chem. Phys. **117**, 6959 (2002).
[27]H. Salis and Y. Kaznessis, J. Chem. Phys. **122**, 054103 (2005).
[28]A. Chatterjee and A. F. Voter, J. Chem. Phys. **132**, 194101 (2010).
[29]E. C. Dybeck, C. P. Plaisance, and M. Neurock, J. Chem. Theory Comput. **13**, 1525 (2017).
[30]M. J. Hoffmann, S. Matera, and K. Reuter, Comput. Phys. Commun. **185**, 2138 (2014).
[31]K. Reuter and M. Scheffler, Phys. Rev. B **73**, 045433 (2006).
[32]M. P. Andersson, F. Abild-Pedersen, I. N. Remediakis, T. Bligaard, G. Jones, J. Engbaek, O. Lytken, S. Horch, J. H. Nielsen, J. Sehested, J. R. Rostrup-Nielsen, J. K. Nørskov, and I. Chorkendorff, J. Catal. **255**, 6 (2008).
[33]P. Giannozzi, S. Baroni, N. Bonini, M. Calandra, R. Car, C. Cavazzoni, D. Ceresoli, G. L. Chiarotti, M. Cococcioni, I. Dabo, A. D. Corso, S. de Gironcoli, S. Fabris, G. Fratesi, R. Gebauer, U. Gerstmann, C. Gougoussis, A. Kokalj, M. Lazzeri, L. Martin-Samos, N. Marzari, F. Mauri, R. Mazzarello, S. Paolini, A. Pasquarello, L. Paulatto, C. Sbraccia, S. Scandolo, G. Sclauzero, A. P. Seitsonen, A. Smogunov, P. Umari, and R. M. Wentzcovitch, J. Phys.: Condens. Matter **21**, 395502 (2009).
[34]Ultrasoft pseudopotentials are taken from the Quantum ESPRESSO pseudopotential library and were generated using the "atomic" code by A. Dal Corso in 2012 (v.5.0.2 svn rev. 9415).
[35]J. Wellendorff, K. T. Lundgaard, A. Møgelhøj, V. Petzold, D. D. Landis, J. K. Nørskov, T. Bligaard, and K. W. Jacobsen, Phys. Rev. B **85**, 235149 (2012).
[36]L. Bengtsson, Phys. Rev. B **59**, 12301 (1999).
[37]G. Henkelman, B. P. Uberuaga, and H. Jonsson, J. Chem. Phys. **113**, 9901 (2000).
[38]S. R. Bahn and K. W. Jacobsen, Comput. Sci. Eng. **4**, 56 (2002).
[39]Z.-J. Zhao, A. Kulkarni, L. Vilella, J. K. Nørskov, and F. Studt, ACS Catal. **6**, 3760 (2016).
[40]*NIST Computational Chemistry Comparison and Benchmark Database, NIST Standard Reference Database Number 101*, edited by R. D. Johnson (National Institute of Standards and Technology, Gaithersburg, MD, 2015).
[41]A. J. Medford, C. Shi, M. J. Hoffmann, A. C. Lausche, S. R. Fitzgibbon, T. Bligaard, and J. K. Nørskov, Catal. Lett. **145**, 794 (2015).
[42]A. Stierle and A. M. Molenbroek, MRS Bull. **32**, 1001–1009 (2007).
[43]M. A. Newton, Chem. Soc. Rev. **37**, 2644 (2008).
[44]K. Reuter, C. P. Plaisance, H. Oberhofer, and M. Andersen, J. Chem. Phys. **146**, 040901 (2017).
[45]J. Nielsen, M. d'Avezac, J. Hetherington, and M. Stamatakis, J. Chem. Phys. **139**, 224706 (2013).
[46]C. Stegelmann, A. Andreasen, and C. T. Campbell, J. Am. Chem. Soc. **131**, 8077 (2009).
[47]S.-C. Li, Z. Zhang, D. Sheppard, B. D. Kay, J. M. White, Y. Du, I. Lyubinetsky, G. Henkelman, and Z. Dohnalek, J. Am. Chem. Soc. **130**, 9080 (2008).
[48]D.-J. Liu, F. Zahariev, M. S. Gordon, and J. W. Evans, J. Phys. Chem. C **120**, 28639 (2016).